GEOFLUIDS

Geofluids (2013) doi: 10.1111/gfl.12030

Deformation bands and their impact on fluid flow in sandstone reservoirs: the role of natural thickness variations

A. ROTEVATN[1], T. H. SANDVE[3], E. KEILEGAVLEN[3], D. KOLYUKHIN[2] AND H. FOSSEN[1,4]

[1]*Department of Earth Science, University of Bergen, Bergen, Norway;* [2]*Centre for Integrated Petroleum Research, Uni Research, Bergen, Norway;* [3]*Department of Mathematics, University of Bergen, Bergen, Norway;* [4]*Natural History Collections, University Museum of Bergen, University of Bergen, Bergen, Norway*

ABSTRACT

Cataclastic deformation bands, which are common in sandstone reservoirs and which may negatively affect fluid flow, are generally associated with notable thickness variations. It has been suggested previously that such thickness variations represent an important control on how deformation bands affect fluid flow. The effects of such thickness variations are tested in this study though statistical analysis and fluid flow simulation of an array of cataclastic deformation bands in Cretaceous sandstones in in the Bassin de Sud-Est in Provence, France. Spatial outcrop data are statistically analyzed for incorporation in flow simulation models, and numerical simulations are used to investigate the effects of notable thickness variations on how the deformation bands influence effective permeability and flow dynamics. A suite of simulations is performed using a combination of fine-scale and coarse-scale grids, revealing that the effective permeability of the simulated reservoir is reduced by a factor of 15–25. More interestingly, the simulations further demonstrated that, as compared to the overall effect of the deformation band array on fluid flow, thickness variations along the bands proved to have negligible effects only. Thus, our simulations indicate that the configuration and connectivity of the deformation bands, together with the permeability contrast between the bands and the host rock and the mean band thickness, are the most important controls on the effective permeability. Our findings represent new insight into the influence of deformation bands on fluid flow in subsurface aquifers and reservoirs, indicating that thickness variations of individual deformation bands are of less significance than previously thought.

Key words: deformation bands, flow baffles, fluid flow, reservoir, sandstone, thickness variations

Received 17 November 2012; accepted 8 March 2013

Corresponding author: A. Rotevatn, Department of Earth Science, University of Bergen, Allégaten 41, 5007 Bergen, Norway.
E-mail: atle.rotevatn@geo.uib.no. Tel: +47 48109959. Fax: +47 55583660.

Geofluids (2013)

INTRODUCTION

In highly porous (porosity >15%) granular rocks, applied stresses yield distinct deformation processes facilitated by availability of pore space. These include: (i) rigid grain reorganization (granular flow) resulting in compaction, dilation or isochoric strain; (ii) grain fracturing/crushing (cataclasis) related to high stress concentrations at grain contact points (Antonellini *et al.* 1994). The resultant strain localization features are generally known as shear bands or deformation bands (Aydin 1978), mm-wide tabular-planar deformation features across which strain is accommodated. *Cataclastic* deformation bands, which are compactional shear bands in which grain crushing has taken place, are favored by high confining pressures (Fossen *et al.* 2007) and good sorting and rounding, which produce high stress concentrations at grain contact points (Gallagher *et al.* 1974). In simple terms, cataclasis is regarded as a common deformation mechanism in porous sandstones having undergone faulting at depths greater than approximately 1 km (Fisher & Knipe 2001). In the following we use the term deformation band exclusively about *cataclastic* deformation bands.

Deformation bands are known to be associated with a reduction in porosity and permeability relative to the host rock in which they occur (Antonellini & Aydin 1994). In groundwater or hydrocarbon aquifers, deformation bands may therefore represent baffles to fluid flow during exploitation, thereby reducing the effective permeability of the reservoir. This has been explored by a range of authors, focusing on the effect of deformation bands on effective permeability (Sternlof *et al.* 2004; Kolyukhin *et al.* 2010),

pressure distribution (Matthäi *et al.* 1998; Rotevatn & Fossen 2011) and flow tortuosity (Rotevatn *et al.* 2009). Several previous workers have noted that faults, including those occurring in porous sandstone, are associated with large variations in *macroscopic fault thickness* (Shipton & Cowie 2001; Shipton *et al.* 2002; Flodin & Aydin 2004). Such variations are generally seen as important controls on the fault sealing characteristics of fault zones (Shipton *et al.* 2005). Other workers have noted that also at a much finer, sub-fault zone scale, *individual deformation bands* are generally characterized by significant variation in thickness in three dimensions (Fossen & Bale 2007; Fossen *et al.* 2007; Torabi & Fossen 2009). The same authors have speculated that the thickness variations may be of significance when considering the effect of deformation bands on fluid flow, and, specifically that thickness minima may undermine the effect of deformation bands as sealing or flow-reducing structures. Despite the fact that deformation bands are common in sandstone aquifers and reservoirs, this potentially crucial aspect of their effect on fluid flow has not previously been quantitatively dealt with in the literature.

In this study we aim to numerically explore the importance of such thickness variations for fluid flow in sandstone reservoirs and aquifers. Specifically, we aim to test and quantify how thickness variations influence the effect of deformation bands on effective permeability and fluid flow dynamics in a fluid extraction situation. Subordinately, the study also addresses the overall effect of the studied deformation band array on effective permeability and fluid flow in the simulated aquifer.

The problem is explored numerically based on statistical data from a deformation band population occurring in contractionally deformed high-porosity Cretaceous sandstones in the central Bassin du Sud-Est, SE France (Wibberley *et al.* 2007; Saillet & Wibberley 2010; Klimczak *et al.* 2011). First, spatial outcrop data are statistically analyzed for incorporation in flow simulation models. Second, a suite of simulations is performed using a combination of fine-scale and coarse-scale grids.

GEOLOGICAL SETTING OF THE STUDY AREA

The studied rock units are sandstones of Cretaceous age in the Quartier de l'Etang quarry near Orange in the central Bassin du Sud-Est, SE France (Fig. 1). The Bassin du Sud-Est is a Mesozoic intra-cratonic basin on the edge of the Alpine orogen, bordered by the Mediterranean Sea to the south, the Alps to the east, and the Massif Central to the northwest. The basin extends c. 200 km by 150–100 km with sediment thicknesses varying from 2 to 3000 m to approximately 10 000 m (Delfaud & Dubois 1984). During (late-stage) and following deposition, the basin was affected by several tectonic events: (i) Late Cretaceous Eoalpine and Pyrenean shortening resulting in folding of Mesozoic strata

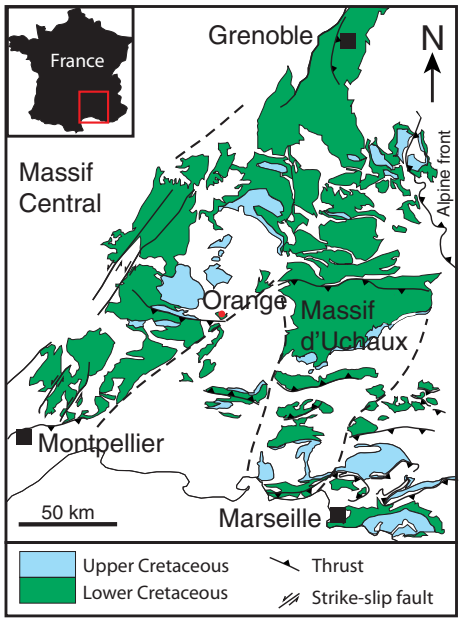

Fig. 1. Geological map of the Bassin du Sud-Est in Provence, France. The studied outcrop in Orange is located in the central basin. Location of the area is shown on the inset map.

and basin inversion (Arthaud & Séguret 1981; Tempier 1987; Séranne *et al.* 1995; Sanchis & Séranne 2000); (ii) Oligocene extension related to the opening of the Gulf of Lion resulting in extensional faulting (Séranne *et al.* 1995; Sanchis & Séranne 2000); and (iii) related Miocene contraction leading to strike-slip reactivation of existing faults (Ford & Stahel 1995; Séranne *et al.* 1995; Saillet & Wibberley 2010). In the study area, limestones and sandstones of Cretaceous age are exposed, significantly affected by the initial Late Cretaceous shortening (Klimczak *et al.* 2011). The studied rocks in the Quartier de l'Etang quarry are medium-grained quartz arenites, representing delta and beach sands deposited in Cenomanian time (Debrand-Passard *et al.* 1984; Wibberley *et al.* 2007). The low maximum burial (800 m, see Delfaud & Dubois 1984) and lack of cementation leaves their initial high porosity preserved.

The studied outcrop in the inactive Quartier de l'Etang quarry (Orange, France) is identical to that studied by Wibberley *et al.* (2007), Saillet & Wibberley (2010) and Klimczak *et al.* (2011). As reported by these authors, arrays of mainly NW-SE striking reverse-sense (i.e. formed during tectonic shortening) deformation bands occur in the high-porous sandstones in the quarry (Fig. 2). An approximately 300 m wide outcropping section was studied, throughout which the deformation bands are persistently present. Saillet & Wibberley (2010) describe the deformation band population as two main sets that are conjugate, implying they formed coevally under the same stress conditions, whereas Klimczak *et al.* (2011) argue

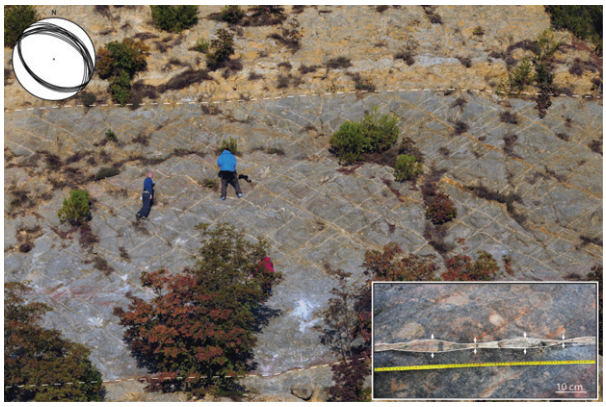

Fig. 2. The studied outcrop in the Quartier de l'Etang quarry in Orange exhibits two oppositely dipping arrays of reverse-sense deformation bands, as shown on the photograph and equal area stereo net. The studied unit is outlined between the white dotted lines and represent arenitic sandstone layer, bounded above and below by calcite cemented sandstone layers containing fewer or no deformation bands. The inset photo shows thickness variations along one of the bands. See text for details.

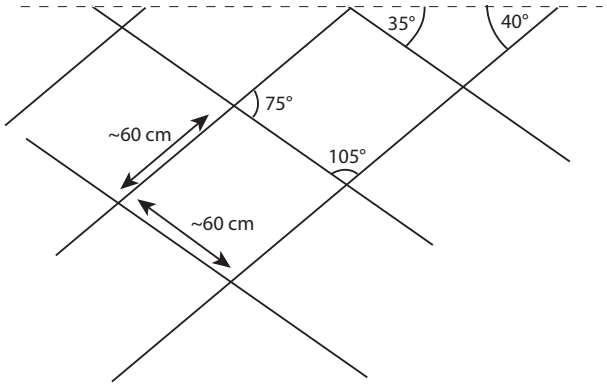

Fig. 3. Generalized scheme of deformation band distribution used in the numerical simulations.

that there are three sets of reverse sense deformation bands that formed sequentially (although under the same overall stress field). We shall not address this discussion in the present contribution, as the main scope herein is to assess their effect on fluid flow. We consider the bands as formed under the same stress field as agreed by both Saillet & Wibberley (2010) and Klimczak *et al.* (2011) and describe two subsets identified in the field without considering their relative timing.

The deformation bands in the studied outcrops are described in detail in Saillet & Wibberley (2010) and we limit ourselves to observations that have implications for the numerical flow simulations. The deformation band array consists of mm- to cm-thick, mostly multistrand deformation bands in two NW-SE striking, but oppositely dipping sets (Fig. 2). The bands exhibit significant cataclastic grain size reduction relative to the host rock, and the bands feature mm- to cm-scale reverse-sense displacement. The deformation bands show notable thickness variability along strike (see inset photo, Fig. 2). This motivates testing the effect of these thickness variations on effective permeability and flow dynamics in the numerical flow simulations. Detailed thickness data were therefore recorded along individual bands, which are presented and analyzed in the next section.

STATISTICAL ANALYSIS OF SPATIAL DATA

To test the overall effect of the deformation band array on fluid flow, the orientation and spacing of the bands must be represented in the model. The orientations of the bands in the model are based on the field measurements of deformation band orientations (Fig. 2). The spacing of deformation bands in the models are based on field measurements of deformation band spacing, but given the desire to highlight the effect of the thickness variations in the simulations, a fixed mean spacing was used. The average spacing between the bands, although somewhat variable on the local scale (Fig. 2), exhibits a quite striking overall consistency throughout the outcropping section. We use 60 cm as an approximation for mean deformation band spacing, representing a low-end conservative estimate to avoid overemphasizing the effect of the deformation bands on fluid flow. The standard deviation σ of the spacing is defined by $3\sigma = 10$ cm. The general scheme for orientation and distribution of deformation bands used in the numerical simulations are shown in Fig. 3.

To address the impact on fluid flow of the thickness variations, an understanding of the variation is needed. Thickness data were collected along three deformation bands, hereafter termed DB1, DB2 and DB3. These are representative for the thickness variations observed across the deformation band array. Thickness was recorded at 1 cm intervals along the deformation bands, and the thickness measurements were measured over a length of 309–750 cm for different bands (see Table 1). The mean dis-

Table 1 Datasets statistics and *P*-values of normality and stationarity checking. T = thickness of deformation bands.

Dataset	DBand1	DBand1a	DBand2	DBand3
Length (cm)	723	309	400	750
Number of measurements *N*	724	310	53	95
Mean (*T*) (cm)	1.94	1.82	0.7	2.68
$\sigma(T)$ (cm)	0.99	0.75	0.44	1.28
Min(*T*) (cm)	0.2	0.2	0.1	0.1
max(*T*) (cm)	7	3.5	1.8	5.7
Lilliefors test *P*-value	0.001	0.001	0.04	0.26
Jarque–Bera test *P*-value	0.001	0.08	0.36	0.41
Leybourne–McCabe test *P*-value	0.1	0.1	0.1	0.01
KPSS test *P*-value	0.01	0.01	0.1	0.01

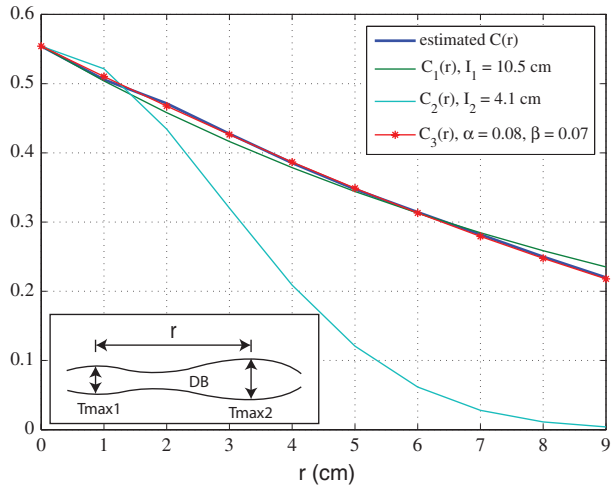

Fig. 4. Estimated correlation function and corresponding analytical approximations for DB1a. As shown in the inset figure, r represents the distance between thickness maxima along deformation bands. DB = deformation band; Tmax = thickness maximum. See text for details.

tance between thickness maxima is 25 cm and the length over which measurements were made therefore well exceeds that necessary to capture the variations in thickness. To facilitate meaningful input parameters to the simulation model, a statistical analysis of the data is necessary. In Table 1, mean values and standard deviations of the thickness are shown for the three bands, together with the maximal and minimal values measured. To investigate the quality of the statistical model and its parameters we test for normality and stationarity; that is if the mean values and variances are constant along the individual bands and the correlation functions depend only on the spatial distance r (see Fig. 4 inset for illustration of r). Because we have relatively few measured data available we consider two tests both for normality and stationarity checking: The Jarque–Bera and Lilliefors tests (Lilliefors 1967; Jarque & Bera 1987) were used for normality checking; and the Leybourne-McCabe (Leybourne & McCabe 1999) and KPSS tests (Kwiatkowski *et al.* 1992) for stationarity. Corresponding P-values and datasets statistics are presented in Table 1. We suppose that the normality or a stationarity holds if the corresponding P-value is > 0.05 at least for one test.

From Table 1 we can see that for each dataset the P-value of at least one test of normality exceeds the usual 5% significance level. It allows us to consider, for simplicity, the thickness $T(x) = \langle T \rangle + T'(x)$ as a stationary normal random function in the sequel. Then its probability distribution can be completely defined by its mean value and covariance function $C(r)$. Furthermore, in this work we only consider the main strand of DB 1 that is DB 1a, as DB 1a better satisfies the normality tests than DB 1. Moreover, we note that stationarity of the third band is broken

Table 2 Parameter values used to define the correlation function C_3.

	DBand1	DBand2	DBand3
α	0.08	0.05	0.04
β	0.07	0.9	0.63

since the dataset is split in two parts along parts of its surveyed length (the band bifurcates into two strands). Therefore we exclude the third band from all simulations that consider upscaling of the permeability.

The covariance can be estimated from measurements by a moving window estimator (Li & Lake 1994). Also we consider three analytical covariance functions (Monin & Yaglom 1975):

$$C_1(r) = \sigma^2 e^{-r/I},$$

$$C_2(r) = \sigma^2 e^{-\pi r^2/(4I^2)},$$

$$C_3(r) = \sigma^2 e^{-\alpha r} \cos \beta r,\ I = \frac{\alpha}{\alpha^2 + \beta^2}$$

Here, σ is the standard deviation, I is the correlation length of the random function, k is the wave number, and the parameters α and β are defined according to Table 2. The use of analytical correlation functions allow us to study how the large scale flow properties of the medium (e.g. permeability) depend on $\langle T \rangle$, σ and I.

In Figs 4 and 5 we present $C(r)$ estimated from DB1a and DB2, respectively. Estimation of $C(r)$ yields a high computational error for large distances r, whereas the approximations are better for smaller values of r. We therefore approximate C_1 in the range $0 \leq r \leq 9$ cm, C_2 and

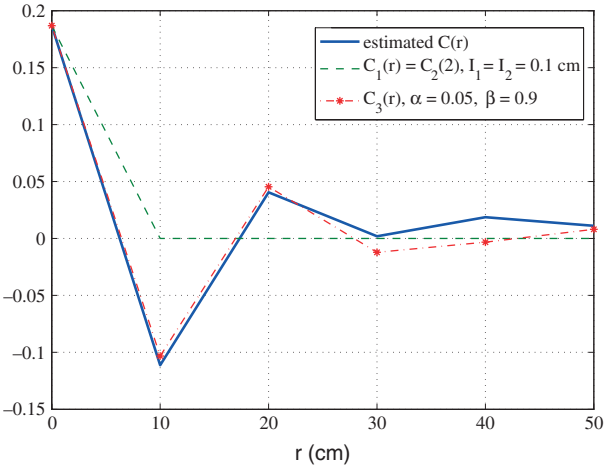

Fig. 5. Estimated correlation function and corresponding analytical approximations for DB2. r represents the distance between thickness maxima along deformation bands (see Fig. 4). See text for details.

Table 3 Correlation lengths and norms related to approximation by $C_1(r)$, $C_2(r)$ and $C_3(r)$.

Dataset	I_1(cm)	$\|C(r)-C_1(r)\|_2$	I_2(cm)	$\|C(r)-C_2(r)\|_2$	I_3(cm)	$\|C(r)-C_3(r)\|_2$
DBand1a	10.5	0.026	4.1	0.126	7.1	0.008
DBand2	0.1	0.12	0.1	0.12	0.06	0.028
DBand3	22.9	0.444	11.4	0.862	0.1	0.454

C_3 in the range $0 \leq r \leq 50$ cm (the values are chosen so that the Frobenius norm of the residuals in the domains fulfil $C(r) \geq C(0)/e$). The correlation lengths and Frobenius norms related to C_1, C_2 (r) and C_3 (r) are shown in Table 3.

The thickness distribution $T(x)$ from dataset DB1a is presented in Fig. 6(A). To indicate the meaning of the different correlation functions, Fig. 6(B–D) show the realizations of random functions related to $C_1(r)$, C_2 (r), and C_3 (r). A simulation formula for the scalar real-valued homogeneous Gaussian random field with the spectral function $S(k)$ is described for example in Sabelfeld (1991). We observe significant differences between the realizations produced by the three estimated statistical distributions. The impact of the different statistical distributions on the bulk permeability is addressed in Section 'Results and Discussion'.

The thickness distribution of DB2 is presented in Fig. 7 (A). In Fig. 7(B–D) we show the realizations of random functions related to C_1 (r), C_2, and C_3 (r) for DB2. It is clear that for this deformation band the simulated T (x) are qualitatively similar for all analytical correlation functions. The negative part of $C(r)$ and small value of I_1, I_2 and I_3 may be caused by less densely spaced data points and poor statistics related to DB2. On the other hand, it means that $T(x)$ values in adjacent points are more independent, and this explains why the realizations presented in 7b–d are rather similar.

For the flow simulations presented in the next few sections, we will populate the simulation domain with bands of different thickness, and in some cases also include thickness variations along individual bands. Based on the available field observations, the deformation bands are assumed to be divided into two thickness distribution families, with statistical properties defined in Tables 1 and 2. Furthermore, assumptions are needed on the distribution of bands between the two families. In addition to the thickness data from the two described deformation bands, the field data include data on the distribution of local thickness maxima and minima from a range of bands at the studied locality. These data are not spatially organized (i.e. not collected systematically along single bands) and we assume that these distributions of maxima and minima are Gaussian. In our simulations, each band has one of two distributions estimated from DB1a and DB2, as described above with probabilities P_1, and P_2, respectively. To estimate these probabilities we estimate two Gaussian probability density functions corresponding to considered datasets. Furthermore, by comparing the values of likelihood functions for

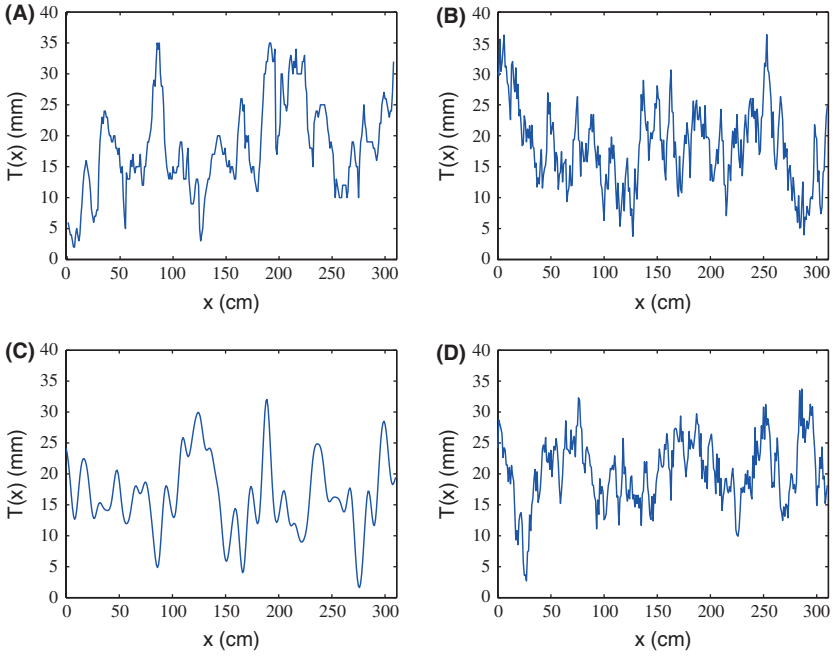

Fig. 6. (A) The recorded thickness distribution along DB1a. (B) Synthetic realization of the stationary normal random function related to C1(*x*) for DB1a. (C) Synthetic realization of the stationary normal random function related to C2(*x*) for DB1a. (D) Synthetic realization of the stationary normal random function related to C3(*x*) for DB1a.

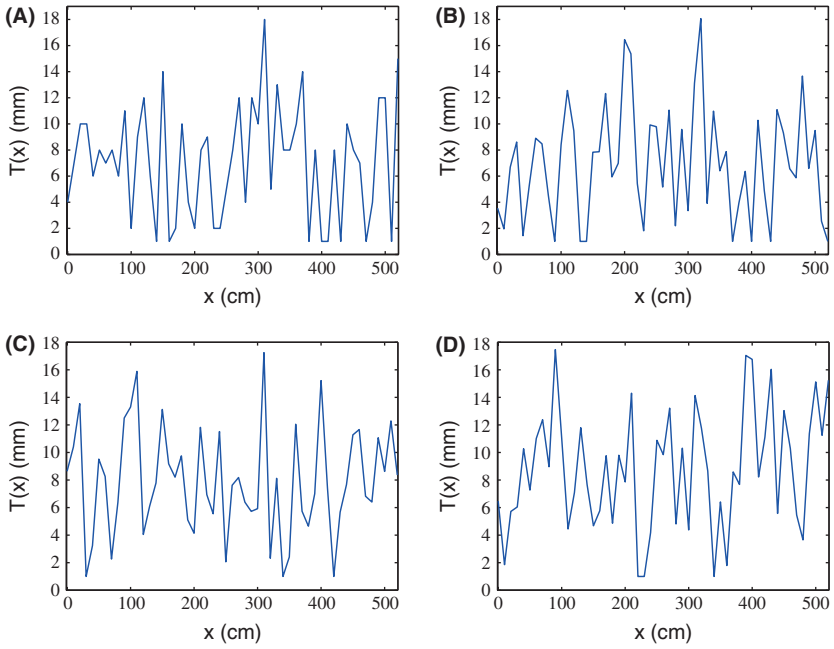

Fig. 7. (A) The recorded thickness distribution along DB2. (B) Synthetic realization of the stationary normal random function related to C1(*x*) for DB2. (C) Synthetic realization of the stationary normal random function related to C2(*x*) for DB2. (D) Synthetic realization of stationary normal random function related to C3(*x*) for DB2.

each disordered measurement we estimate $P_1 = 0.41$ and $P_2 = 0.59$. Note that parameters of similar Gaussian mixture model can also be estimated by Expectation Maximization algorithm (EM). We emphasize the uncertainty in these estimates; however, they do provide a distribution that can be applied in the simulation model. To improve the quality of the statistical analyses and to provide more accurate estimates on the modelling parameters, more data are needed.

NUMERICAL SIMULATION MODEL

To assess the impact of the studied deformation bands on fluid flow we turn to numerical simulations. The motivation for the simulations is twofold: First, simulations on small domains with bands represented with (i) uniform thickness; and (ii) thickness variations illustrate the impact of the bands on the fine-scale fluid distribution. Second, upscaling of the strained rock to an effective permeability allows us to estimate the impact of the deformation bands on the field (outcrop) scale of observation.

Setup

All simulations consider a case of water injection into a two-dimensional vertical cross section of a reservoir that is initially filled with oil. To isolate the effects of deformation bands, thickness variations, and permeability contrasts, both fluids are modeled as incompressible, phase transitions are not considered and we assume no capillary pressure between the phases. With these assumptions the pressure equation reads

$$-\nabla \cdot \boldsymbol{K} \nabla h = 0,$$

where $\boldsymbol{K}$ represents the permeability and h is the hydraulic head. There are no source terms in the domain, the flow is instead driven by boundary conditions as described below. The water saturation S_W is transported according to the equation

$$\phi \frac{\partial S_W}{\partial t} + \nabla \cdot (\boldsymbol{q} f_W + \boldsymbol{K} \lambda_0 f_W (\rho_0 - \rho_W) \boldsymbol{g}) = 0,$$

where ϕ is the porosity, $\boldsymbol{q} = -\boldsymbol{K} \nabla h$ is the Darcy velocity, λ_α is the mobility of phase α and $f_W = \frac{\lambda_W}{\lambda_W + \lambda_0}$ is the fractional flow function. Furthermore, ρ_α is the density of phase α and $\boldsymbol{g}$ is the gravity vector.

The densities are set to 1000 kg m^{-3} for the water phase and 700 kg m^{-3} for the oil phase. The phase viscosities are 5 cp for water and 1 cp for oil, and the relative permeabilities are quadratic with zero residual saturation. Water is injected along the entire left hand side of the domain and the fluids are allowed to flow out of the right hand side. Along the top and bottom of the domain no-flow conditions are assigned.

The rock model consists of a homogenous host rock with deformation bands, and the distribution and geometry of the bands are based on the statistical analyses of collected field data presented in the previous section. That is,

the bands are configured according to Fig. 3, and their statistical properties are set according to Table 1 and 2. Host rock and deformation band permeabilities are set constant to 500 and 0.5 mD based on probe permeameter measurements in the field (see Rotevatn *et al.* 2008 for details about the measurement tools and methods). This is in accordance with previously published figures (see Fossen *et al.* 2007 and references therein) for deformation band permeabilities, which are known to be associated with permeabilities 1–6 orders of magnitude (most studies reporting 2–4 orders of magnitude) less than that of the host rock. Finally, the porosity is set to 0.25 and 0.07 for the host rock and the deformation bands, respectively.

Discretization

A key challenge associated with investigating the effect of deformation bands on fluid flow is their small width relative to their length. The computational cost associated with explicitly resolving the bands in a field-scale simulation model will be prohibitively high. Thus, a natural goal for the investigations is to upscale the deformation bands. To achieve this, high-resolution simulation studies of the bands are necessary.

To resolve the deformation bands, the computational grid should conform to the bands, and to achieve this, triangular cells are appealing due to their flexibility. In this grid, there are essentially two ways to represent the deformation bands. The first option is to assign cells inside the bands in what can be termed an equi-dimensional approach. When considering the band aspect ratio, we realize that a second option is to consider the bands as lower dimensional objects (lines in 2D, or planes in 3D). This leads to a hybrid approach where the deformation bands are lines in the geometric grid, but correctly represented with their width in the simulation model. The hybrid approach both simplifies the grid generation and excludes small cells in the intersection of the deformation bands, yielding a more robust and efficient discretization compared to standard equi-dimensional approaches (Karimi-Fard *et al.* 2004; Sandve *et al.* 2012). The hybrid approach was originally designed for simulating fractured porous media; however, it has also successfully been applied to compaction bands (Sternlof *et al.* 2006).

In this work an equi-dimensional approach is followed for the fine-scale simulations presented in the next section. The equi-dimensional approach allows for an exact representation of the thickness variations along the deformation bands and is therefore suitable for the fine-scale study. For permeability upscaling and large scale simulations the hybrid method is appropriate. The simplicity and robustness of the hybrid gridding algorithm makes the hybrid method an attractive choice for the permeability upscaling as a multiple of grid realizations are necessary in order to quantify the permeability. For large scale simulations an equi-dimensional approach is too computationally demanding. On these grids, the pressure equation is discretized with a class of control volume methods that can handle skewed cells (Edwards & Rogers 1998; Aavatsmark 2002), while upstream weighting is applied for water transport (Aziz & Settari 1979). Both the pressure and the transport equations are solved implicitly using sequential splitting; that is in each time step, the pressure equation is solved first, then the transport equation. The simulations are performed partly using the toolkit described in Lie *et al.* (2012).

RESULTS AND DISCUSSION

Fine-scale simulations

To illustrate the qualitative impact of thickness variations, we first consider fine-scale simulations on a domain with size 3×3 m. The small size allows us to study the fine-scale impact of the bands as well as to resolve the thickness variations along individual bands. Because DB3 had the most pronounced variations, we include this band even though we do not have reliable data on their spatial distribution. Thus the simulations in this section should not be used for quantitative estimates, but they do give clear illustrations of the effect of the deformation bands on the fluid flow.

Consider Fig. 8(A,B), where the bands are represented with uniform thickness (the thickness varies between bands, but no thickness variations along individual bands are included here). The figures show that the bands hinder the water flow; the water flows easily through the host rock, while it is delayed when it needs to break through a low-permeable band. The impact of the different families of bands is also clear: the front propagation is slowest in the lowermost part of the domain, where the water has to cross many thick bands. Also note the thick bands running diagonally through the domain (from approximately [0, 0.4] to [3, 2.6]), which forces the water to flow upwards, and produce the farthest front propagation.

Next, we consider the same domain with thickness variations along individual bands included, as shown in Fig. 8 (C,D). In this example, the thickness variations are constructed using the correlation function $C_I(x)$ (see Section 'Statistical Analysis of Spatial Data'). By comparing Fig. 8 (B,D), we see that the speed of the water front is indistinguishable for the cases without and with thickness variations. Fig. 8(D) also indicates the much finer grid needed to resolve the thickness variations. To emphasize the very fine-scale impact of the thickness variations, Fig. 9 shows a zoom in of the saturations in Fig. 8(D), together with the associated streamlines. Both figures show that the water tends to

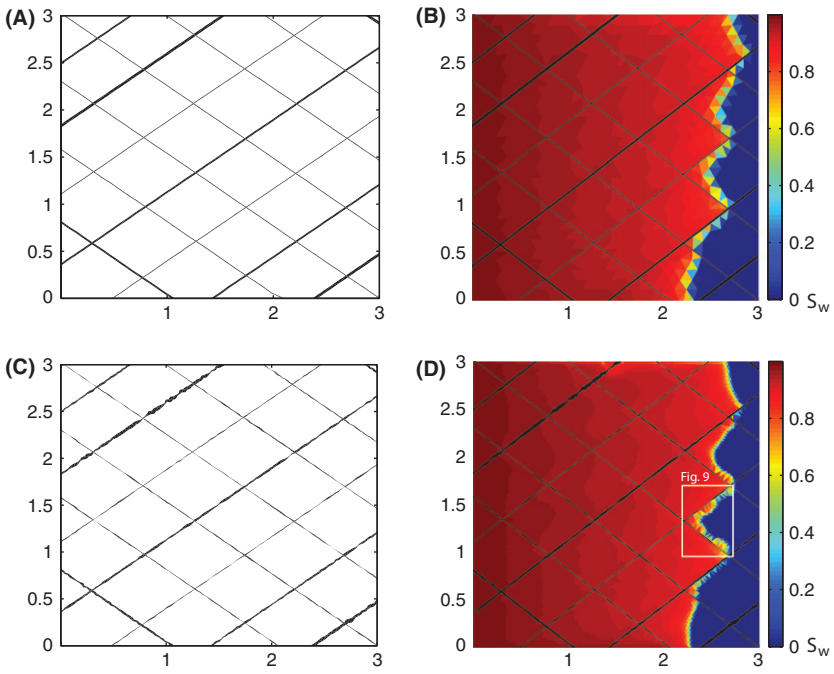

Fig. 8. The figure shows the band distribution (A and C) and water saturation (S_w) profiles (B and D) for domains without (A and B) and with (C and D) variations in thickness along individual deformation bands included. The direction of flow is from left to right in the figure. The white box indicates the area shown in Fig. 9.

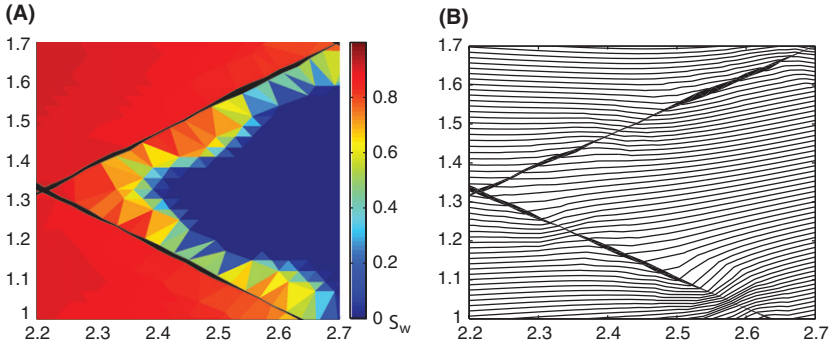

Fig. 9. Illustrations of the local impact of variations of thickness on (A) water saturation (S_w) and (B) streamlines. The figure is zoomed in on Fig. 8(D) on a part of the domain which exhibits large thickness variations. The *x*- and *y*-axes correspond with those in Fig. 8(D). The direction of flow is from left to right in the figure. See Fig. 8(D) for the location of this part of the domain.

break through the thinnest parts of the deformation bands, while the flow density is smaller around the thickness maxima of the low-permeable bands.

To summarize, the fine-scale simulations indicate that deformation bands have an impact on fluid flow. Variations along the thickness of individual bands produce differences on the localization of cross-band flow at the scale of individual bands; however, they do not produce significant differences in the front propagation speed even on the scale of the present relatively small domain (3 m × 3 m).

Permeability upscaling

As seen in the previous section, computational grids that resolve the fine-scale structure of the deformation bands can provide a good picture of the fine-scale distribution of fluids. However, the computational cost associated with simulations on these grids may be prohibitively high for larger domains. It is therefore of interest to compute an effective permeability to be able to incorporate the effect of the low-permeable bands without the need to represent them explicitly on a reservoir scale.

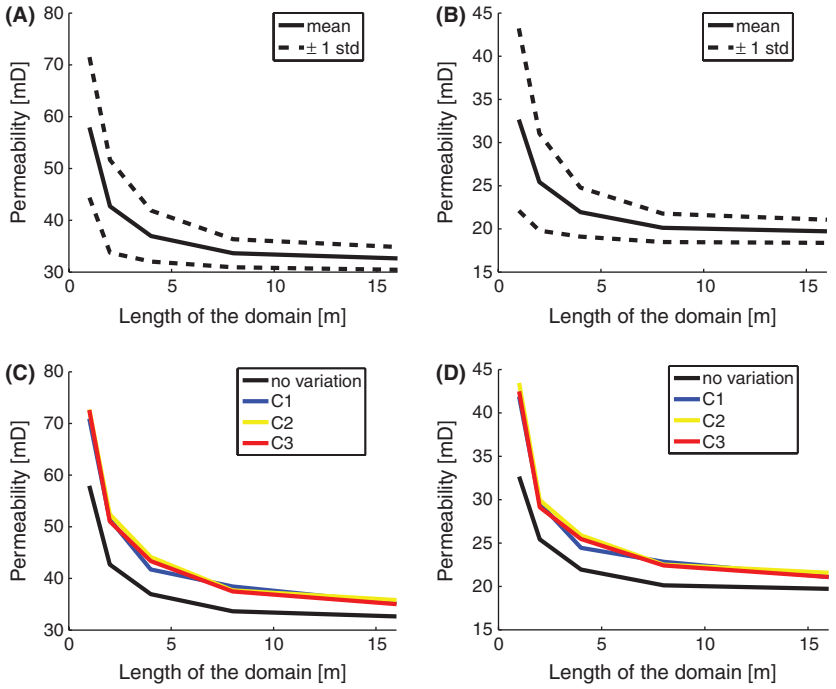

Fig. 10. Upscaled permeabilities as a function of the size of the averaging domain. (A) and (B) show the mean and the standard deviations in both *X* (a) and *Y* (b) directions for 100 realizations of domains with no thickness variations along individual bands. (C) and (D) compare the means of cases with (C) and without (D) variations along the deformation bands, using the different correlation functions described in the text.

The effective permeability of a domain will depend on the properties of the deformation bands that populate the domain. On small averaging domains, the upscaled permeability may be highly variable due to the small sample size of deformation bands, but we expect the variations to decrease as the size of the target domain increases. We therefore consider a series of domains with increasing size, where each domain is populated with 100 different realizations of deformation bands. For each individual grid, an effective permeability is computed using constant no-flow boundary conditions on two opposite sides, and flow is driven between the two other sides. This simple technique is sufficient to obtain an estimate of the upscaled permeability. For more information on upscaling methods, see for instance Renard & de Marsily (1997) and Durlofsky (2005). We emphasize that in these calculations only DB1a and DB2 are considered.

Figure 10(A, B) show the resulting mean and standard deviations for the upscaled permeability in the x and y directions, respectively (no thickness variation along individual bands included). The high values for the smallest domain sizes are probably caused by there being so few deformation bands that there are still high-permeable pathways between the domain boundaries. For larger domains sizes, the curves flatten, and the standard deviation decreases. On the largest domain mean values of $k_x = 32.6$ and $k_y = 19.7$ mD are obtained. The permeability is lowest in the y-direction, because the geometric configuration of the deformation bands is such that the band density is higher along the *y*-axis. Compared to the host rock, the deformation bands thus reduce the permeability with a factor of order 15–25, depending on the geometric configuration of the bands.

Now, consider Fig. 10(C,D). These compare the upscaled permeability for deformation bands with thickness variations along individual bands, and for the different correlation functions presented in Section 'Statistical Analysis of Spatial Data'. For ease of comparison, the corresponding results without variations are also shown. We observe that the thickness variations serve to increase the upscaled permeability with a factor of up to 20%. An increase in the upscaled permeability was to be expected, since the fine-scale simulations showed that the fluid prefers to cross the thinnest parts of the deformation bands, this will result in an increased effective permeability. Compared to the alteration in the upscaled permeability from the introduction of deformation bands in the host rock, the thickness variations have only minor impact. Moreover, the significant differences in the deformation band thickness that might arise when applying different correlation functions (confer Fig. 6) are not reflected in the upscaled permeability. Furthermore, additional simulations (not shown here) for a large range of σ and I failed to produce more than minor differences in the effective permeability. We note that the effect of the thickness variations can also be achieved by a small, uniform reduction in the band thickness, but due to

the sparseness in the measurements, we have not found such a data fitting exercise worthwhile.

For simplicity, the geometry of the deformation bands has been kept constant throughout the upscaling experiments, except from the minor variability in the spacing between the bands. This is also in agreement with the field observations. However, the upscaling on small domains gives an indication what the effective permeability will be for domains with relatively few bands, and thus a higher probability of there being highly permeable pathways across the domain. As observed from Fig. 10, this band sparseness has a large impact on the permeability. Thus, our simulations indicate that the configuration and connectivity of the deformation bands, together with the permeability contrast between the bands and the host rock and the mean band thickness are the most important parameters for the effective permeability.

We remark that the fairly simple approach to upscaling explored here is made possible from the geometrical arrangement of the deformation bands. The two oppositely dipping populations of deformation bands are assumed to have equal statistical properties, producing a symmetry in the problem, and an upscaled permeability that is aligned with our (x,y) coordinate system. This also means that for the simulation scenarios considered herein with the deformation bands symmetrically distributed with respect to the main flow paths, the bands will not serve to rotate the flow on the large scale; individual outliers have minor impact. This will not hold true if there are systematic differences between the two families of bands producing different statistical properties, and more advanced upscaling techniques would have been necessary to compute effective permeabilities in this case.

Large-scale simulation

The permeability upscaling provides parameters for a coarse simulation model. To assess the quality of the upscaling, we perform simulations on a 200 m × 30 m domain, with both the fine-scale grid and Cartesian coarse-scale grid with 40 × 6 cells. To resolve the thickness variations along individual bands on this domain is far too costly; even without the variations, the fine-scale grid has almost a million elements. We therefore neglect thickness variations for all deformation bands. In the fine-scale grid, deformation bands are resolved discretely and permeability values assigned to the bands and host rock using identical values as the small scale models described above (500 mD host rock permeability, 0.5 mD deformation band permeability). To the Cartesian grid, we assign the upscaled permeability found from the corresponding upscaling (k_x = 32.6 and k_y = 19.7 mD), while the porosity is set to 0.2431; computed as the volume weighted mean of the deformation band and host rock values. In these simulations, hydrostatic pressure is set both on the left and right hand side. We consider a pressure drop of 500 bars across the domain.

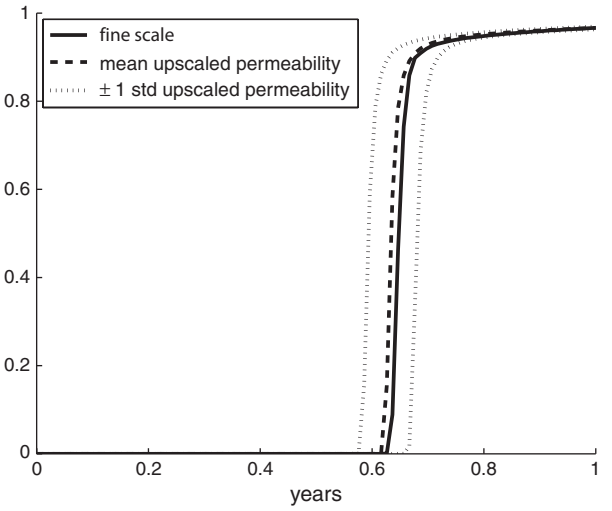

Fig. 11. Coarse- (Cartesian grid) and fine-scale (triangular grid) water cut curves for the large domain (200 m by 30 m). The coarse-scale simulation is performed with the mean upscaled permeability, as well as permeabilities one standard deviation above and below the mean (cf. Fig. 10A). See text for details.

Figure 11 shows the water cut curves for both the coarse-scale and the fine-scale solution with the high pressure drop. We observe that the breakthrough time is very similar for the two simulations. Moreover, the curves also indicate the same behavior after the breakthrough. This confirms that the permeability upscaling is meaningful also for larger domains.

Summary and applicability of results

Deformation bands are naturally occurring deformation structures that baffle fluid flow in subsurface sandstone aquifers and reservoirs (Antonellini & Aydin 1994). Recent work has shown that deformation bands are typified by variations in thickness along individual bands (Fossen & Bale 2007; Torabi & Fossen 2009) and suggested that this may impact the way in which deformation bands affect fluid flow. The above-described results provide a quantitative examination of the effect of such variations for a particular field example.

In general, the fine-scale simulations of deformation bands with *thickness variations* produced no significant difference compared to the fine-scaled simulations with *constant deformation bands thickness*. Streamlines did however show that the thickness variation has some effect on the scale of individual deformation bands, in that fluids tend to flow across the deformation bands at thickness minima. Yet, even on the scale of the fine-scale simulations (3 × 3 meters simulation domain), this effect was not reflected in an overall difference in waterfront propagation.

Numerical upscaling of effective permeability showed that thickness variations lead to a somewhat increased effective permeability (Fig. 10). However, compared to the overall reduction in permeability inflicted by the introduction of the deformation band array in the host rock, the impact of the thickness variations is minor. This contrasts what is known for macroscopic fault zones, where previous work has shown that effective cross-fault permeability is sensitive to fault thickness changes (Shipton *et al.* 2002).

These results indicate that, contrary to what has been suggested qualitatively by previous studies, thickness variations are of negligible importance when considering the effect of deformation bands on fluid flow in subsurface aquifers or petroleum reservoirs. This is important because (i) deformation bands are common and affect fluid flow in sandstone reservoirs (Harper & Moftah 1985; Edwards *et al.* 1993; Lewis & Couples 1993; Hesthammer & Fossen 2001), ; and (ii) an appropriate and quantitative understanding and representation of deformation bands is crucial for optimal management of sandstone aquifers and reservoirs in which they occur (Rotevatn *et al.* 2009). This study addresses the latter point, indicating that thickness variations along individual deformation bands are of minor importance and therefore not necessary to account for when considering fluid flow in subsurface sandstone aquifers and reservoirs. Furthermore, the results from the large scale simulations demonstrate that permeability upscaling is meaningful for implicitly representing deformation band arrays on an aquifer scale, and that discrete (and computationally expensive) representation of deformation bands is made redundant. It is stressed that while this holds true for the relatively simple geometrical arrangement of the deformation band array studied herein, geometrically complex arrays of deformation bands may have effects on fluid flow (such as effects on flow tortuosity) that would require a more sophisticated three-dimensional approach (Rotevatn & Fossen 2011).

The results from this study warrant some comments on the applicability and limitations of the results presented herein. The results should be treated with some caution given the simplifications assumed when representing the bands in the simulations. The complexity of the deformation band arrays in the studied outcrop is not fully captured in the model. Nevertheless, insofar as the true abundance, distribution, and connectivity of the bands are underrepresented in the simulations, the substantial flow and transport effects realized here can reasonably be considered as conservative, low-end estimates. Also on a cautionary note is our two-dimensional approach to this inherently three-dimensional problem. However, field observations indicate that the bands are laterally extensive and thus, given a pressure gradient, fluids will cross the domain in a manner that may be approximated in two dimensions. We therefore consider the two-dimensional approach as a fair approximation of the three-dimensional problem, although flow tortuosity effects are not fully captured and would need a three-dimensional approach to be fully understood.

CONCLUSIONS

It has been the purpose of this study to address numerically how deformation band arrays and, particularly, their inherent thickness variations influence effective permeability and flow dynamics in porous sandstone aquifers. Fluid flow simulations were preformed based on statistical data collected from a naturally occurring deformation band array in Cretaceous sandstones of the Bassin du Sud-Est in Provence, France. Our results showed that the studied array of deformation bands reduced the effective permeability of the simulated aquifer by a factor of 15–25. However, as we demonstrate numerically, the thickness variations proved to have negligible effects only, as compared to the overall effect of the deformation band array on fluid flow: thickness variations along the deformation bands only negligibly influenced the modification of effective permeability, and had no detectable effect on waterfront propagation in the small-scale simulations. Given this finding, we conclude that (i) thickness variations may have minor effects on flow paths across individual deformation bands; (ii) thickness variations may affect the effective permeability to some extent for small sample sizes (less than approximately 5 m simulation length in this study); (iii) thickness variations have little or no effect on effective permeability and flow dynamics on a reservoir scale; and (iv) the configuration and connectivity of the deformation bands, together with the permeability contrast between the bands and the host rock and the mean band thickness, are the most important controls on the effective permeability and flow dynamics in sandstone aquifers.

Finally, we stress that the findings of this study have implications for resource management in subsurface sandstone aquifers and reservoirs. While thickness variations proved to have little or no effect on fluid flow, the magnitude of permeability reduction exerted by the band array in the simulations demonstrate that accounting for such band fabrics could prove essential to the optimal management of sandstone aquifers and reservoirs in which they occur. Numerical upscaling represents a meaningful method to represent and account for the mm-scale bands in reservoir models, which would otherwise have to be represented discretely at a high computational cost.

ACKNOWLEDGEMENTS

Roger Soliva is thanked for directing us to the outcrops in the Quartier de l'Etang quarry. The Centre for Integrated Petroleum Research (Uni CIPR, Uni Research) is acknowl-

edged for funding the field work associated with this study. The financial support from Statoil-VISTA, research cooperation between the Norwegian Academy of Science and Letters and Statoil, to the fourth author is acknowledged. His research was carried out as part of the Impact of Fault Envelope Architecture on Reservoir Fluid Flow Project at Uni CIPR, Uni Research. Eivind Bastesen, Sylvie Schueller and Sigurd Fossen are thanked for collaboration and company in the field. Two anonymous reviewers are thanked for their constructive and encouraging reviews. This work was conducted within the COPS (Contractional deformation Of Porous Sandstones) project at Uni CIPR.

REFERENCES

Aavatsmark I (2002) An introduction to multipoint flux approximations for quadrilateral grids. *Computational Geosciences*, **6**, 405–32.

Antonellini M, Aydin A (1994) Effect of faulting on fluid flow in porous sandstones: petrophysical properties. *AAPG Bulletin*, **78**, 355–77.

Antonellini M, Aydin A, Pollard DD (1994) Microstructure of deformation bands in porous sandstones at Arches National Park, Utah. *Journal of Structural Geology*, **16**, 941–59.

Arthaud F, Séguret A (1981) Les structures pyrénéennes du Languedoc et du Golfe du Lion (Sud de la France). *Bulletin de la Societe Geologique de France* **XXIII**, 51–63.

Aydin A (1978) Small faults formed as deformation bands in sandstone. *Pageoph*, **116**, 913–30.

Aziz K, Settari A (1979) *Petroleum Reservoir Simulation*. Applied Science Publishers Ltd, London.

Debrand-Passard S, Courbouleix S, Lienhardt MJ (1984) Synthèse géologique du Sud-Est de la France, Stratigraphie et paléogéographie. *Mémoires du Bureau de Recherches Geologiques et Minières (BRGM), Orleans, France* **125**, 615.

Delfaud J, Dubois P (1984) Le bassin du Sud-Est. In: *Dynamique des bassins sédimentaires. Livre jubilaire BRGM* (ed. Gubler Y), pp. 347–61. BRGM, Orleans, France.

Durlofsky LJ (2005) Upscaling and gridding of fine scale geological models for flow simulation. In: 8th International Forum on Reservoir Simulation, Iles Borromees, Stresa, Italy, June 20–24, 2005, available at: http://pangea.stanford.edu/ERE/research/suprihw/durlofsky/upsc_grid_review_ifrs_2005.pdf.

Edwards MG, Rogers CF (1998) Finite volume discretization with imposed flux continuity for the general tensor pressure equation. *Computational Geosciences*, **2**, 259–90.

Edwards HE, Becker AD, Howell JA (1993) Compartmentalization of an aeolian sandstone by structural heterogeneities: permo-Triassic Hopeman Sandstone, Moray Firth, Scotland. In: *Characterization of Fluvial and Aeolian Reservoirs* (eds North CP, Prosser DJ). *Geological Society, London, Special Publications* **73**, 339–66.

Fisher QJ, Knipe RJ (2001) The permeability of faults within siliciclastic petroleum reservoirs of the North Sea and Norwegian Continental Shelf. *Marine and Petroleum Geology*, **18**, 1063–81.

Flodin E, Aydin A (2004) Faults with asymmetric damage zones in sandstone, Valley of Fire State Park, southern Nevada. *Journal of Structural Geology*, **26**, 983–8.

Ford M, Stahel U (1995) The geometry of a deformed carbonate slope-basin transition: the Ventoux-Lure fault zone, SE France. *Tectonics*, **14**, 1393–410.

Fossen H, Bale A (2007) Deformation bands and their influence on fluid flow. *AAPG Bulletin*, **91**, 1685–700.

Fossen H, Schultz RA, Shipton ZK, Mair K (2007) Deformation bands in sandstone - a review. *Journal of the Geological Society, London*, **164**, 755–69.

Gallagher JJ, Friedman M, Handin J, Sowers GM (1974) Experimental studies relating to microfracture in sandstone. *Tectonophysics*, **21**, 203–47.

Harper TR, Moftah I (1985) Skin effect and completion options in the Ras Budran Reservoir. *SPE Middle East Oil Technical Conference and Exhibition*, **13708**, 211–26.

Hesthammer J, Fossen H (2001) Structural core analysis from the Gullfaks area, northern North Sea. *Marine and Petroleum Geology*, **18**, 411–39.

Jarque CM, Bera AK (1987) A test for normality of observations and regression residuals. *International Statistical Review*, **55**, 163–72.

Karimi-Fard M, Durlofsky LJ, Aziz K (2004) An efficient discrete-fracture model applicable for general-purpose reservoir simulators. *SPE Journal*, **9**, 227–36.

Klimczak C, Soliva R, Schultz RA, Chéry J (2011) Sequential growth of deformation bands in a multilayer sequence. *Journal of Geophysical Research*, **116**, B09209.

Kolyukhin D, Schueller S, Espedal M, Fossen H (2010) Deformation band populations in fault damage zone—impact on fluid flow. *Computational Geosciences*, **14**, 231–48.

Kwiatkowski D, Phillips PCB, Schmidt P, Shin Y (1992) Testing the null hypothesis of stationarity against the alternative of a unit root: how sure are we that economic time series have a unit root? *Journal of Econometrics*, **54**, 159–78.

Lewis H, Couples GD (1993) Production evidence for geological heterogeneities in the Anschutz Ranch East Field, western USA. In: *Characterization of Fluvial and Aeolian Reservoirs* (eds North CP, Prosser DJ). *Geological Society, London, Special Publications* **73**, 321–38.

Leybourne SJ, McCabe BPM (1999) Modified stationarity tests with data-dependent model-selection rules. *Journal of Business & Economic Statistics*, **17**, 264–70.

Li D, Lake LW (1994) A moving window semivariance estimator. *Water Resources Research*, **30**, 1479–89.

Lie KA, Krogstad S, Ligaarden I, Natvig J, Nilsen H, Skaflestad B (2012) Open-source MATLAB implementation of consistent discretisations on complex grids. *Computational Geosciences*, **16**, 297–322.

Lilliefors HW (1967) On the Kolmogorov–Smirnov test for normality with mean and variance unknown. *Journal of the American Statistical Association*, **62**, 399–402.

Matthäi SK, Aydin A, Pollard DD, Roberts SG (1998) Numerical simulation of departures from radial drawdown in a faulted sandstone reservoir with joints and deformation bands. In: *Faulting, Fault Sealing and Fluid Flow in Hydrocarbon Reservoirs* (eds Jones G, Fisher QJ, Knipe RJ). *Geological Society, London, Special Publications*, **147**, 157–91.

Monin AS, Yaglom AM (1975) *Statistical Fluid Mechanics (Vol II): Mechanics of Turbulence*. MIT Press, Cambridge.

Renard P, de Marsily G (1997) Calculating equivalent permeability: a review. *Advances in Water Resources*, **20**, 253–78.

Rotevatn A, Fossen H (2011) Simulating the effect of subseismic fault tails and process zones in a siliciclastic reservoir analogue: implications for aquifer support and trap definition. *Marine and Petroleum Geology*, **28**, 1648–62.

Rotevatn A, Torabi A, Fossen H, Braathen A (2008) Slipped deformation bands: a new type of cataclastic deformation bands

in Western Sinai, Suez rift, Egypt. *Journal of Structural Geology*, **30**, 1317–31.

Rotevatn A, Tveranger J, Howell JA, Fossen H (2009) Dynamic investigation of the effect of a relay ramp on simulated fluid flow: geocellular modelling of the Delicate Arch Ramp, Utah. *Petroleum Geoscience*, **15**, 45–58

Sabelfeld KK (1991) *Monte Carlo Methods in Boundary Value Problems*. Springer, New York/Heidelberg/Berlin.

Saillet E, Wibberley CAJ (2010) Evolution of cataclastic faulting in high-porosity sandstone, Bassin du Sud-Est, Provence, France. *Journal of Structural Geology*, **32**, 1590–608.

Sanchis E, Séranne M (2000) Structural style and tectonic evolution of a polyphase extensional basin of the Gulf of Lion passive margin: the Tertiary Alès basin, southern France. *Tectonophysics*, **322**, 219–42.

Sandve TH, Berre I, Nordbotten JM (2012) An efficient multi-point flux approximation method for Discrete Fracture–Matrix simulations. *Journal of Computational Physics*, **231**, 3784–800.

Séranne M, Benedicto A, Labaum P, Truffert C, Pascal G (1995) Structural style and evolution of the Gulf of Lion Oligo-Miocene rifting: role of the Pyrenean orogeny. *Marine and Petroleum Geology*, **12**, 809–20.

Shipton ZK, Cowie PA (2001) Damage zone and slip surface evolution over μm to km scales in high-porosity Navajo sandstone, Utah. *Journal of Structural Geology*, **23**, 1825–44.

Shipton ZK, Evans JP, Robeson KR, Forster CB, Snelgrove S (2002) Structural heterogeneity and permeability in faulted aeolian sandstone: implication for subsurface modeling of faults. *AAPG Bulletin*, **86**, 863–83.

Shipton ZK, Evans JP, Thompson LB (2005) The geometry and thickness of deformation-band fault core and its influence on sealing characteristics of deformation-band fault zones. In: *Faults, Fluid Flow and Petroleum Traps* (eds Sorkhabi R, Tsuji Y.) *AAPG Memoir*, **85**, 181–95.

Sternlof KR, Chapin JR, Pollard DD, Durlofsky LJ (2004) Permeability effects of deformation band arrays in sandstone. *AAPG Bulletin*, **88**, 1315–29.

Sternlof KR, Karimi-Fard M, Pollard DD, Durlofsky LJ (2006) Flow and transport effects of compaction bands in sandstone at scales relevant to aquifer and reservoir management. *Water Resources Research*, **42**, W07425.

Tempier C (1987) Modèle nouveau de mise en place des structures provençales. *Bulletin de la Societe Geologique de France*, **8**, 533–40.

Torabi A, Fossen H (2009) Spatial variation of microsturcture and petrophysical properties along deformation bands in reseervoir sandstones. *AAPG Bulletin*, **93**, 919–38.

Wibberley CAJ, Petit J-P, Rives T (2007) The mechanics of fault distribution and localization in high-porosity sands, Provence, France. In: *The Relationship between Damage and Localization* (eds Couples GD, Lewis H) *The Geological Society of London, Special Publications*, **289**, 19–46.